

Cross-calibration of the *Rosetta* Navigation Camera based on images of the 67P comet nucleus

Thiago Statella^{1★} and Bernhard Geiger^{2★}

¹Instituto Federal de Educação, Ciência e Tecnologia de Mato Grosso, 95 Zulmira Canavarro, 780025-200, Brazil

²Aurora Technology B.V., ESA/ESAC, Camino bajo del Castillo s/n, E-28692 Villanueva de la Cañada, Spain

Accepted 2017 June 21. Received 2017 May 18; in original form 2017 March 27

ABSTRACT

The *Rosetta* spacecraft carried a Navigation Camera (NavCam) for optical navigation in the vicinity of the comet. In order to facilitate the use of the data for quantitative scientific work, we performed a cross-calibration study based on images taken with the OSIRIS near-angle camera. For this purpose, we selected sets of images acquired roughly simultaneously on 2014 August 1 during comet approach at small phase angles. We employed two procedures, the first one based on the average signal over the nucleus and the second considering histograms of signal values within the images. Both methods delivered consistent results for the radiometric calibration factor. As a first application and further consistency check, we employed the calibration procedure to an extended set of NavCam images acquired at phase angles ranging from $\sim 1^\circ$ to 55° in order to study the nucleus reflectance properties. From empirical model fits to the phase angle dependence we obtained values of 0.065 ± 0.003 for the geometric albedo and 0.019 ± 0.001 for the Bond albedo in the broad spectral sensitivity band of the camera.

Key words: techniques: image processing – techniques: photometric – comets: individual: 67P/Churyumov–Gerasimenkov.

1 INTRODUCTION

The *Rosetta* spacecraft encountered its target comet 67P/Churyumov–Gerasimenkov in 2014 August and escorted it through the perihelion passage until 2016 September when the mission ended by landing the spacecraft on the nucleus. In addition to a series of scientific instruments, the spacecraft also carried a Navigation Camera (NavCam) for operational purposes. NavCam images were scheduled by the Rosetta Flight Dynamics team located at the European Space Operations Centre. Analysis of these images was essential for determining the spacecraft position with respect to the comet nucleus and hence for safely navigating *Rosetta*. The techniques applied for optical navigation during the comet approach phases were documented by Castellini et al. (2015) and methods used near the comet, primarily based on the observation of landmarks, by Pardo de Santayana & Lauer (2015). The former paper also describes empirical photometric models used for estimating the appropriate exposure time for image acquisition.

The images provided by the NavCam are also of great interest for the scientific community. Applications include the usage as context images (e.g. Feldman et al. 2015) or the study of comet outbursts (e.g. Grün et al. 2016, Vincent et al. 2016). During the operational project phases, uncalibrated images were distributed in near real time (Geiger 2016) to the Rosetta instrument team community

via the Science Ground Segment located at the European Science Astronomy Centre. In addition, corresponding product data sets were regularly delivered to the Planetary Science Archive (PSA) for long-term preservation. The main camera parameters and image product characteristics are summarized in the data set documentation available in the archive (Geiger, Barthelemy & Archibald 2016).

Accurate geometric information was required for the operational objective of the NavCam and the respective image characteristics are therefore well established. However, less effort has been made by the manufacturer on the characterization of the radiometric properties. As a consequence, data sets of radiometrically calibrated images have not been available so far. Geiger et al. (in preparation) report relevant and available technical information about the NavCam instrument in detail and describe the results of point source calibration studies. Furthermore, that paper includes an extensive discussion of image artefacts and methods for their correction, as well as a documentation of the processing steps carried out for generating calibrated image product data sets.

In this publication, we present cross-calibration studies based on images acquired by the scientific camera system OSIRIS (Keller et al. 2007; Sierks et al. 2015). More specifically, we used radiometrically calibrated images of the OSIRIS narrow-angle camera (NAC) in order to determine multiplicative calibration factors for the conversion of NavCam image counts into physical radiance units. As a consistency check, we applied the radiometric calibration to an extended set of images and studied the phase angle dependence of the reflectance properties.

* E-mail: thiago.statella@cba.ifmt.edu.br (TS); bernhard.geiger@esa.int (BG)

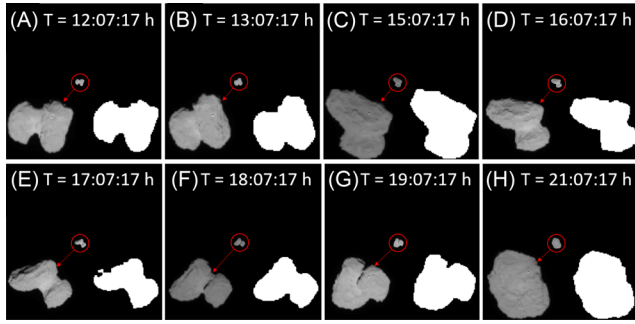


Figure 1. NavCam images acquired on 2014 August 1, at times ranging from $t = 12:07:17$ h to $t = 21:07:17$ h. A zoomed inset of the comet nucleus is shown at the bottom left corner of each image, and the binary mask used to segment pixels belonging to the comet nucleus is shown at the bottom right corner of each figure. The dynamic range of the images has been enhanced for better visualization. The time of acquisition for each image is given on the top of the scenes. More information about the images is given in Table 1. Credits: ESA/Rosetta/NavCam. Archive data set: Geiger & Barthelemy (2015).

2 CROSS-CALIBRATION OF THE NAVCAM IMAGES WITH OSIRIS DATA

We followed two different approaches for the cross-calibration study. In the first one, we have considered a disc-integrated methodology using the average comet nucleus signal in the calculations. For that purpose, we extracted the digital number (DN) values of pixels laying in the comet nucleus with a binary mask for marking the nucleus limb. Hence, we are referring to this approach as the mask-based one. Next, we have performed an analysis considering the whole range of intensity values as recorded by the camera. We refer to that as the histogram-based approach. Both treatments have led us to consistent results, which support the reliability of the estimated parameters. We show our results in the next sections, Section 2.1 for the mask-based and Section 2.2 for the histogram-based method.

The selection of images used for the study was based on the following criteria:

- (i) The phase angle shall be small in order to assure that the visible part of the nucleus surface is well illuminated and the occurrence of shadows is minimal.
- (ii) The distance of the spacecraft shall be such that the nucleus is fully contained in the field of view of both NavCam and OSIRIS-NAC (lower limit on the distance).
- (iii) The distance shall be such that the nucleus extends over a sufficient number of pixels in the OSIRIS-NAC and NavCam images (upper limit on the distance).

(iv) NavCam images and OSIRIS-NAC filter sequences need to be available with small differences in acquisition time in order to minimize changes owing to the comet rotation.

(v) The images should be acquired early in the mission at a large Sun distance in order to avoid or minimize potential contributions to the measured signal caused by an active coma.

2.1 Mask-based estimations

The NavCam images used for this study were acquired by *Rosetta* on 2014 August 1 in the time range from $T = 12:07:17$ h to $T = 21:07:17$ h. The data are available in ESA's PSA as uncalibrated 'Level 2' images in PDS3 format (Geiger & Barthelemy 2015). The set of eight available images is presented in Fig. 1, which displays the original images, a zoomed inset of the comet nucleus (at the bottom left corner) and the binary mask used to segment the pixels of the nucleus (at the bottom right corner). Information about these images is given in Table 1. The integration time for each scene was 1.0 s.

As a pre-processing step, we subtracted a bias field from each scene to correct the detector offset. The procedure for generating the bias field is detailed in Geiger et al. (in preparation). Next, we converted the images from DN count numbers to DN per second (DN s^{-1}) by dividing them by the respective scene exposure time T_e . To sum up, the pre-processed images were obtained by applying equation (1):

$$I_C = \frac{(I_o - Bias)}{T_e}, \quad (1)$$

where I_C is the pre-processed image, I_o is the original image, $Bias$ the bias field and T_e is the exposure time in seconds. Note that there are different bias fields applicable depending on the gain settings used (HIGH or LOW gain). The images used for cross-calibration were all acquired with HIGH gain and with the focused attenuated (FOC_ATT) element in the camera optics. The abbreviations in capital letters are the same as used in the archived product files (Geiger et al. 2016).

Binary masks for the comet nucleus were created by using Otsu's algorithm (Otsu 1979) for automatic thresholding. Next, morphological opening and closing transformations, which act as local adaptive filters, were applied to the segmentation in order to filter out black and white isolated pixels caused by noise or artefacts during the acquisition process. Finally, a morphological erosion, which produces a shrinking effect on the brighter objects, was applied to each mask for avoiding the influence of pixels in the fringe of the nucleus when calculating the average nucleus digital number per second (DN s^{-1}). In all morphological transformations, we have used a square spatial filter element with a 3×3 pixel box size.

Table 1. Information on the NavCam images presented in Fig. 1.

| ID | Mode | Gain | Time (hh:mm:ss) | Average signal (DN s^{-1}) | σ (DN s^{-1}) |
|-------------------------------|---------|------|--------------------|--|------------------------------------|
| ROS_CAM1_20140801T120717F.FIT | FOC_ATT | HIGH | 12:07:17 | 1876 | ± 168 |
| ROS_CAM1_20140801T130717F.FIT | FOC_ATT | HIGH | 13:07:17 | 1864 | ± 153 |
| ROS_CAM1_20140801T150717F.FIT | FOC_ATT | HIGH | 15:07:17 | 1764 | ± 162 |
| ROS_CAM1_20140801T160717F.FIT | FOC_ATT | HIGH | 16:07:17 | 1719 | ± 225 |
| ROS_CAM1_20140801T170717F.FIT | FOC_ATT | HIGH | 17:07:17 | 1759 | ± 242 |
| ROS_CAM1_20140801T180717F.FIT | FOC_ATT | HIGH | 18:07:17 | 1791 | ± 210 |
| ROS_CAM1_20140801T190717F.FIT | FOC_ATT | HIGH | 19:07:17 | 1787 | ± 177 |
| ROS_CAM1_20140801T210717F.FIT | FOC_ATT | HIGH | 21:07:17 | 1733 | ± 125 |

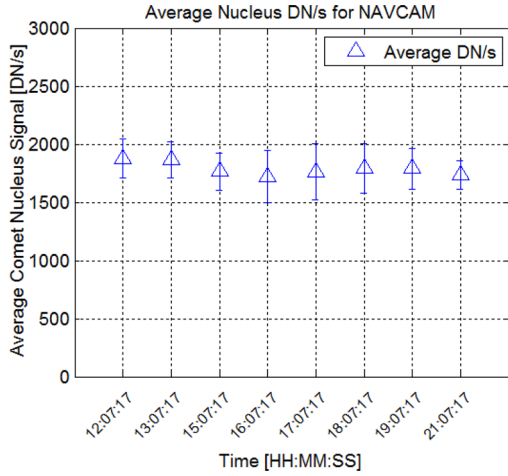


Figure 2. Average comet nucleus signal in DN s^{-1} calculated for the NavCam images. The vertical bars denote the standard deviation (σ) for each image. The numerical values are listed in Table 1.

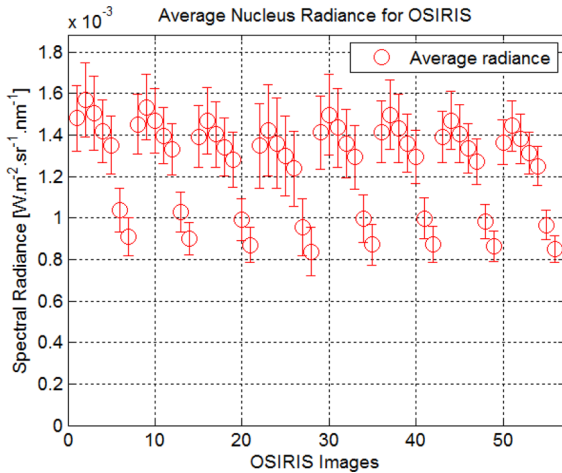


Figure 3. Average comet nucleus spectral radiance L_λ for eight sets of OSIRIS-NAC images close in time to the NavCam images. The vertical bars represent the standard deviation. Each set is composed of seven images taken with different filters corresponding to different spectral bands (in order of acquisition): orange, green, blue, hydra, red, near infrared (NIR) and infrared (IR). Detailed information about the OSIRIS-NAC images is given in Table 2.

For detailed information of the morphological transformations, we refer the reader to Serra (1982).

Fig. 2 shows the resulting average comet nucleus DN s^{-1} for the NavCam images. The average DN s^{-1} and the standard deviation (σ) are presented in Table 1. The dispersion is caused by surface features and shadows, which however are not very prominent, thanks to the selection of images at low phase angle.

For the comparison, we used OSIRIS-NAC images acquired on 2014 August 1 from $T = 11:50:14.576 \text{ h}$ to $T = 20:44:43.524 \text{ h}$, which were radiometrically calibrated as described by Tubiana et al. (2015). The calibrated images are available as ‘Level 3’ data sets in the PSA (Gutierrez-Marques et al. 2015). Fig. 3 shows the average comet nucleus spectral radiance L_λ (in $\text{W m}^{-2} \text{ sr}^{-1} \text{ nm}^{-1}$) and the vertical bars represent its standard deviation. There are eight sets of OSIRIS images which are each composed of seven scenes acquired

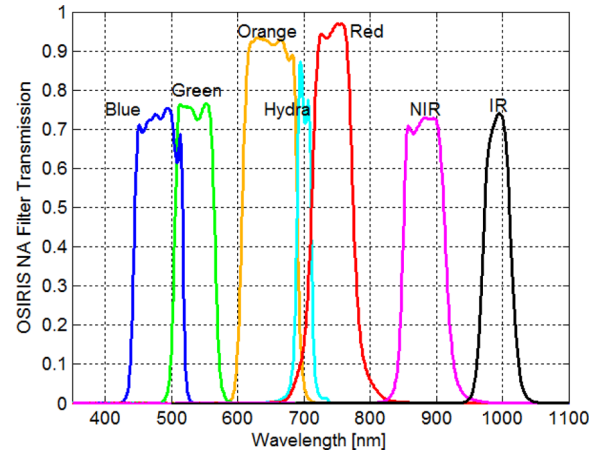


Figure 4. OSIRIS-NAC filter transmission curves for the seven spectral bands: blue, centred at 480.7 nm with bandwidth 74.9 nm; green, centred at 535.7 nm with bandwidth 62.4 nm; orange, centred at 649.2 nm with bandwidth 84.5 nm; hydra, centred at 701.2 nm with bandwidth 22.1 nm; red, centred at 743.7 nm with bandwidth 64.1 nm; NIR, centred at 882.1 nm with bandwidth 65.9 nm; and IR, centred at 989.3 nm with bandwidth 38.2 nm (adapted from Keller et al. 2007; Tubiana et al. 2015).

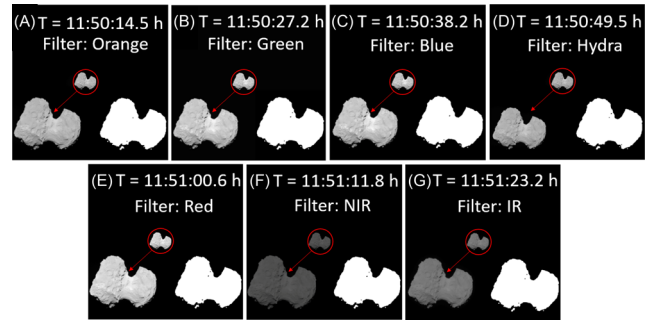


Figure 5. OSIRIS-NAC images and their respective time of acquisition. At the bottom left corner, the figures show a zoomed inset of the comet nucleus and, at the bottom right corner, the mask used to segment pixels belonging to the nucleus. The dynamic range of the images has been enhanced for better visualization. Credits: ESA/Rosetta/MPS for OSIRIS Team MPS/UPD/LAM/IAA/SSO/INTA/UPM/DASP/IDA. Archive data set: Gutierrez-Marques et al. (2015).

in different filters: blue, green, orange, hydra, red, NIR and IR. The transmission curves of the filters are shown in Fig. 4 (Keller et al. 2007; Tubiana et al. 2015). Each set of OSIRIS-NAC data has been chosen to be the closest in acquisition time to the NavCam images. The set whose acquisition time is 11:50 h is shown in Fig. 5. Fig. 5A through Fig. 5G shows the images taken using the filters orange, green, blue, hydra, red, NIR and IR. At the bottom left corner, a zoomed inset of the nucleus is shown and, at the bottom right corner, the mask is shown which was used to isolate only those pixels belonging to the comet nucleus. The procedure to create the masks is the same as used for NavCam images. A summary of the OSIRIS-NAC images is given in Table 2.

For each of the sets of OSIRIS-NAC images, we fitted a third-degree polynomial to the radiance data points in the different filters in order to obtain the spectral radiance distribution $L_o(\lambda)$. Then, we

Table 2. Information on the OSIRIS-NAC images whose comet nucleus average spectral radiances L_λ were calculated and presented in Fig. 3.

| ID | Time (hh:mm:ss) | L_λ ($10^{-3}\text{Wm}^{-2}\text{sr}^{-1}\text{nm}^{-1}$) | σ ($10^{-3}\text{Wm}^{-2}\text{sr}^{-1}\text{nm}^{-1}$) |
|--|--------------------|--|---|
| NAC_2014-08-01T11.50.14.576Z_ID20_1397549800_F82.FIT | 11:50:14.576 | 1.481 | ± 0.158 |
| NAC_2014-08-01T11.50.27.296Z_ID20_1397549900_F23.FIT | 11:50:27.296 | 1.569 | ± 0.179 |
| NAC_2014-08-01T11.50.38.231Z_ID20_1397549000_F24.FIT | 11:50:38.231 | 1.503 | ± 0.178 |
| NAC_2014-08-01T11.50.49.599Z_ID20_1397549100_F27.FIT | 11:50:49.599 | 1.418 | ± 0.151 |
| NAC_2014-08-01T11.51.00.652Z_ID20_1397549200_F28.FIT | 11:51:00.652 | 1.350 | ± 0.140 |
| NAC_2014-08-01T11.51.11.807Z_ID20_1397549300_F41.FIT | 11:51:11.807 | 1.039 | ± 0.105 |
| NAC_2014-08-01T11.51.23.297Z_ID20_1397549400_F71.FIT | 11:51:23.297 | 0.909 | ± 0.090 |
| NAC_2014-08-01T13.20.42.586Z_ID20_1397549500_F82.FIT | 13:20:42.586 | 1.452 | ± 0.142 |
| NAC_2014-08-01T13.20.55.356Z_ID20_1397549600_F23.FIT | 13:20:55.356 | 1.534 | ± 0.157 |
| NAC_2014-08-01T13.21.06.286Z_ID20_1397549700_F24.FIT | 13:21:06.286 | 1.468 | ± 0.155 |
| NAC_2014-08-01T13.21.17.651Z_ID20_1397549800_F27.FIT | 13:21:17.651 | 1.396 | ± 0.134 |
| NAC_2014-08-01T13.21.28.711Z_ID20_1397549900_F28.FIT | 13:21:28.711 | 1.331 | ± 0.125 |
| NAC_2014-08-01T13.21.39.871Z_ID20_1397549000_F41.FIT | 13:21:39.871 | 1.027 | ± 0.095 |
| NAC_2014-08-01T13.21.51.356Z_ID20_1397549100_F71.FIT | 13:21:51.356 | 0.900 | ± 0.080 |
| NAC_2014-08-01T14.43.48.548Z_ID20_1397549200_F82.FIT | 14:43:48.548 | 1.391 | ± 0.148 |
| NAC_2014-08-01T14.44.01.268Z_ID20_1397549300_F23.FIT | 14:44:01.268 | 1.467 | ± 0.160 |
| NAC_2014-08-01T14.44.12.198Z_ID20_1397549400_F24.FIT | 14:44:12.198 | 1.402 | ± 0.156 |
| NAC_2014-08-01T14.44.23.558Z_ID20_1397549500_F27.FIT | 14:44:23.558 | 1.341 | ± 0.140 |
| NAC_2014-08-01T14.44.34.618Z_ID20_1397549600_F28.FIT | 14:44:34.618 | 1.279 | ± 0.133 |
| NAC_2014-08-01T14.44.45.773Z_ID20_1397549700_F41.FIT | 14:44:45.773 | 0.991 | ± 0.102 |
| NAC_2014-08-01T14.44.57.279Z_ID20_1397549800_F71.FIT | 14:44:57.279 | 0.869 | ± 0.085 |
| NAC_2014-08-01T16.08.14.576Z_ID20_1397549900_F82.FIT | 16:08:14.576 | 1.347 | ± 0.202 |
| NAC_2014-08-01T16.08.27.296Z_ID20_1397549000_F23.FIT | 16:08:27.296 | 1.423 | ± 0.220 |
| NAC_2014-08-01T16.08.38.221Z_ID20_1397549100_F24.FIT | 16:08:38.221 | 1.360 | ± 0.217 |
| NAC_2014-08-01T16.08.49.588Z_ID20_1397549200_F27.FIT | 16:08:49.588 | 1.298 | ± 0.193 |
| NAC_2014-08-01T16.09.00.806Z_ID20_1397549300_F28.FIT | 16:09:00.806 | 1.237 | ± 0.182 |
| NAC_2014-08-01T16.09.11.974Z_ID20_1397549400_F41.FIT | 16:09:11.974 | 0.956 | ± 0.138 |
| NAC_2014-08-01T16.09.23.471Z_ID20_1397549500_F71.FIT | 16:09:23.471 | 0.837 | ± 0.116 |
| NAC_2014-08-01T17.26.34.546Z_ID20_1397549600_F82.FIT | 17:26:34.546 | 1.412 | ± 0.177 |
| NAC_2014-08-01T17.26.47.321Z_ID20_1397549700_F23.FIT | 17:26:47.321 | 1.497 | ± 0.194 |
| NAC_2014-08-01T17.26.58.251Z_ID20_1397549800_F24.FIT | 17:26:58.251 | 1.434 | ± 0.190 |
| NAC_2014-08-01T17.27.09.611Z_ID20_1397549900_F27.FIT | 17:27:09.611 | 1.358 | ± 0.164 |
| NAC_2014-08-01T17.27.20.677Z_ID20_1397549000_F28.FIT | 17:27:20.677 | 1.293 | ± 0.154 |
| NAC_2014-08-01T17.27.31.997Z_ID20_1397549100_F41.FIT | 17:27:31.997 | 0.997 | ± 0.116 |
| NAC_2014-08-01T17.27.43.487Z_ID20_1397549200_F71.FIT | 17:27:43.487 | 0.871 | ± 0.099 |
| NAC_2014-08-01T18.31.34.556Z_ID20_1397549900_F82.FIT | 18:31:34.556 | 1.415 | ± 0.148 |
| NAC_2014-08-01T18.31.47.332Z_ID20_1397549000_F23.FIT | 18:31:47.332 | 1.497 | ± 0.166 |
| NAC_2014-08-01T18.31.58.267Z_ID20_1397549100_F24.FIT | 18:31:58.267 | 1.433 | ± 0.165 |
| NAC_2014-08-01T18.32.09.628Z_ID20_1397549200_F27.FIT | 18:32:09.628 | 1.360 | ± 0.140 |
| NAC_2014-08-01T18.32.20.692Z_ID20_1397549300_F28.FIT | 18:32:20.692 | 1.295 | ± 0.129 |
| NAC_2014-08-01T18.32.31.847Z_ID20_1397549400_F41.FIT | 18:32:31.847 | 0.998 | ± 0.097 |
| NAC_2014-08-01T18.32.43.327Z_ID20_1397549500_F71.FIT | 18:32:43.327 | 0.874 | ± 0.086 |
| NAC_2014-08-01T19.37.34.577Z_ID20_1397549200_F82.FIT | 19:37:34.577 | 1.390 | ± 0.125 |
| NAC_2014-08-01T19.37.47.347Z_ID20_1397549300_F23.FIT | 19:37:47.347 | 1.469 | ± 0.141 |
| NAC_2014-08-01T19.37.58.282Z_ID20_1397549400_F24.FIT | 19:37:58.282 | 1.406 | ± 0.140 |
| NAC_2014-08-01T19.38.09.807Z_ID20_1397549500_F27.FIT | 19:38:09.807 | 1.336 | ± 0.119 |
| NAC_2014-08-01T19.38.20.867Z_ID20_1397549600_F28.FIT | 19:38:20.867 | 1.273 | ± 0.110 |
| NAC_2014-08-01T19.38.32.028Z_ID20_1397549700_F41.FIT | 19:38:32.028 | 0.983 | ± 0.083 |
| NAC_2014-08-01T19.38.43.673Z_ID20_1397549800_F71.FIT | 19:38:43.673 | 0.863 | ± 0.072 |
| NAC_2014-08-01T20.43.34.579Z_ID20_1397549900_F82.FIT | 20:43:34.579 | 1.365 | ± 0.107 |
| NAC_2014-08-01T20.43.47.348Z_ID20_1397549000_F23.FIT | 20:43:47.348 | 1.443 | ± 0.121 |
| NAC_2014-08-01T20.43.58.279Z_ID20_1397549100_F24.FIT | 20:43:58.279 | 1.381 | ± 0.120 |
| NAC_2014-08-01T20.44.09.653Z_ID20_1397549200_F27.FIT | 20:44:09.653 | 1.313 | ± 0.100 |
| NAC_2014-08-01T20.44.20.863Z_ID20_1397549300_F28.FIT | 20:44:20.863 | 1.251 | ± 0.093 |
| NAC_2014-08-01T20.44.32.028Z_ID20_1397549400_F41.FIT | 20:44:32.028 | 0.966 | ± 0.071 |
| NAC_2014-08-01T20.44.43.524Z_ID20_1397549500_F71.FIT | 20:44:43.524 | 0.850 | ± 0.062 |

computed the average spectral radiance L_N^* in the NavCam filter band with the NavCam spectral sensitivity curve $S_N(\lambda)$ as follows:

$$L_N^* = \frac{\int_\lambda L_o(\lambda) S_N(\lambda) \lambda d\lambda}{\int_\lambda S_N(\lambda) \lambda d\lambda}. \quad (2)$$

Fig. 6 depicts the sensitivity curve for the NavCam sensor as modelled in Geiger et al. (in preparation). The maximum of the spectral sensitivity is located between 620 and 650 nm and its half-width ranges from approximately 505 to 865 nm. The additional

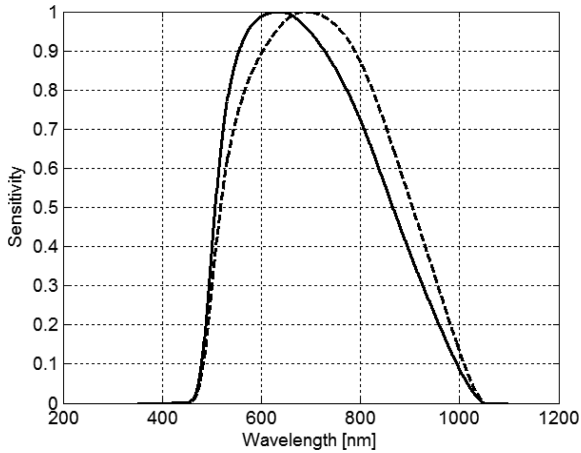


Figure 6. Normalized sensitivity curve (solid line) for the NavCam as modelled in Geiger et al. (in preparation). The dashed curve shows the (normalized) effective spectral sensitivity resulting from the multiplication with the wavelength as relevant for a photon-counting device.

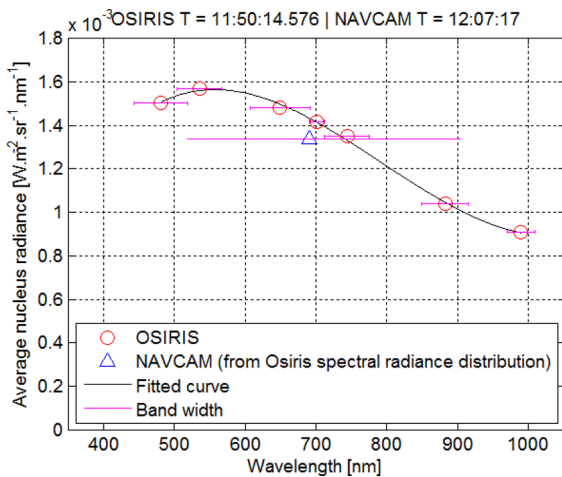


Figure 7. Average comet nucleus spectral radiance as a function of wavelength. Circles represent the OSIRIS-NAC images whereas triangles represent the average spectral radiance in the NavCam band estimated from the spectral radiance distribution derived from the OSIRIS data. The plain black line shows the third-degree polynomial which has been used to fit the OSIRIS-NAC data points. The horizontal bars represent the bandwidth of each filter. On the top of the figure, we give the acquisition time for the first OSIRIS spectral band of the set and for the NavCam image.

weighting by the wavelength λ in equation (2) is necessary in order to take into account that the CCD detector is a photon-counting device. For this reason, the maximum of the effective spectral sensitivity $S_N(\lambda)\lambda$ is shifted to a larger wavelength of ~ 690 nm and the half-width range from 520 to 905 nm.

In Fig. 7, we show the average comet nucleus spectral radiance as a function of wavelength for the first set of images (OSIRIS at $T = 11:50:15$ h and NavCam at $T = 12:07:17$ h). The circles represent the OSIRIS-NAC images whereas triangles represent the NavCam radiance calculated with equation (2) from the spectral radiance distribution derived from the calibrated OSIRIS-NAC images.

As a final step, the NavCam radiometric calibration factor Cal resulting from the cross-calibration exercise can be determined as the ratio of the average spectral radiance L_N^* calculated from

equation (2) and the measured average comet nucleus signal in $DN s^{-1}$:

$$Cal = \frac{L_N^*}{DN s^{-1}}. \quad (3)$$

Table 3 summarizes the L_N^* values for each of the NavCam images as determined from the corresponding set of OSIRIS-NAC images and the resulting calibration factor estimates in $Wm^{-2} sr^{-1} nm^{-1}/(DN s^{-1})$. Taking the average of the values obtained for each of the NavCam images results in a radiometric calibration factor of

$$Cal = (7.14 \pm 0.07) \times 10^{-7} Wm^{-2} sr^{-1} nm^{-1}/(DN s^{-1}). \quad (4)$$

As these images were acquired in attenuated cover position (FOC_ATT) and HIGH gain (see Table 1), the estimated factor is suitable for that specific mode of operation. The corresponding calibration factors for images acquired in other modes will be discussed in the paper by Geiger et al. (in preparation).

Therefore, in order to convert the NavCam DN counts into spectral radiance values (in $Wm^{-2} sr^{-1} nm^{-1}$), the procedure is the following:

$$L_N = Cal \frac{I_0 - Bias}{T_e}, \quad (5)$$

where Cal is the radiometric calibration factor, T_e is the integration time in seconds and $Bias$ is the proper bias field chosen according to the gain settings applied.

In the next section, we present the procedure to estimate the radiometric calibration factor for the NavCam based on the intensity distribution of the scenes.

2.2 Histogram-based estimations

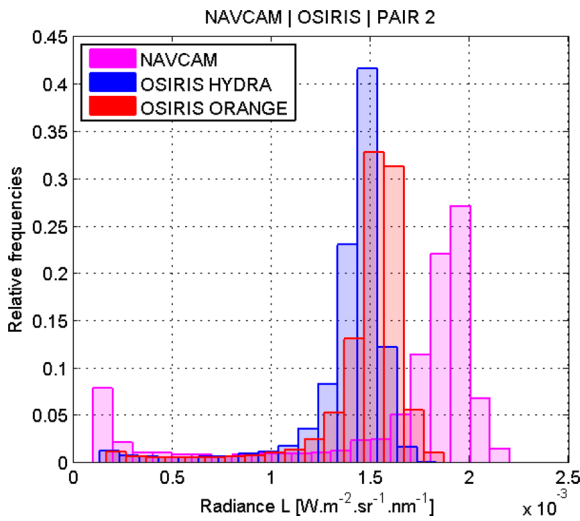
When estimating the radiometric calibration factor for the NavCam by using the average comet nucleus intensity, the results could be influenced by the definition and accuracy of the binary mask, even though we have taken care to avoid the contribution of pixels in the fringe of the mask by applying a morphological erosion to it. Hereafter, we describe the approach based on the DN value distribution of the scenes rather than the average comet nucleus DN.

Fig. 8 shows the histogram for one of the NavCam images converted into spectral radiances by applying a provisional radiometric calibration factor of $1 \times 10^{-6} Wm^{-2} sr^{-1} nm^{-1}/(DN s^{-1})$ that was initially obtained from stellar calibrations (Geiger et al., in preparation) before starting this cross-calibration exercise. This figure also includes histograms for the OSIRIS images in orange and hydra bands from the image set closest in acquisition time. The orange and hydra bands were chosen for being the closest ones to the maximum of the effective NavCam spectral sensitivity distribution. The histogram bins are $10^{-4} Wm^{-2} sr^{-1} nm^{-1}$ wide and are the same for all images. The relative frequencies (vertical axis) were calculated by the ratio between each bin number and the total number of valid pixels in the image. Since the comet nucleus covers only a small area in the fields of view, there is a very high contribution at the dark part of the histograms, which has been cut off in the histograms for all the scenes.

As it can be seen in Fig. 8, the histograms for NavCam and OSIRIS bands do not align with each other, neither in frequency nor in radiance, due to the different wavelengths involved and mainly due to the rough initial calibration factor applied to the NavCam data which needs to be refined in this exercise. There are also small differences between the two OSIRIS histograms owing

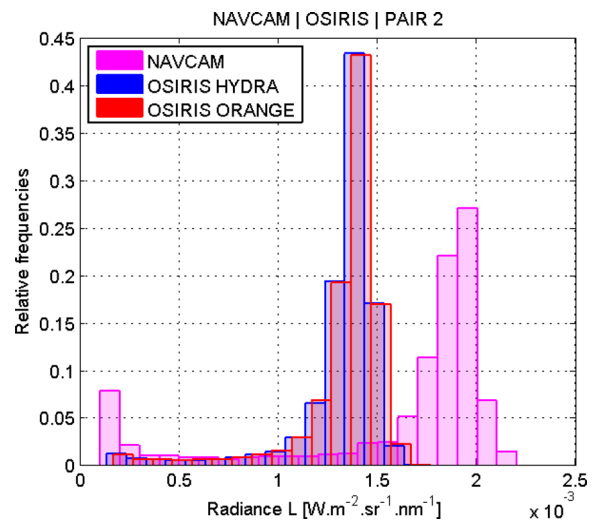
Table 3. Average comet nucleus radiances for NavCam images as estimated with equation (2) and the corresponding calibration factor value for each NavCam image.

| ID | L_N^* ($10^{-3} \text{Wm}^{-2} \text{sr}^{-1} \text{nm}^{-1}$) | Cal [$10^{-7} \text{Wm}^{-2} \text{sr}^{-1} \text{nm}^{-1} / (\text{DN s}^{-1})$] |
|-------------------------------|---|--|
| ROS_CAM1_20140801T120717F.FIT | 1.339 | 7.133 |
| ROS_CAM1_20140801T130717F.FIT | 1.317 | 7.063 |
| ROS_CAM1_20140801T150717F.FIT | 1.264 | 7.167 |
| ROS_CAM1_20140801T160717F.FIT | 1.223 | 7.115 |
| ROS_CAM1_20140801T170717F.FIT | 1.280 | 7.277 |
| ROS_CAM1_20140801T180717F.FIT | 1.282 | 7.157 |
| ROS_CAM1_20140801T190717F.FIT | 1.260 | 7.051 |
| ROS_CAM1_20140801T210717F.FIT | 1.238 | 7.145 |

**Figure 8.** Histograms for one NavCam image converted into spectral radiance by applying a provisional radiometric calibration factor of $\sim 1 \times 10^{-6}$ in $\text{Wm}^{-2} \text{sr}^{-1} \text{nm}^{-1} / (\text{DN s}^{-1})$ (in magenta), for the OSIRIS orange band and for the OSIRIS hydra band. The example NavCam image was taken at $T = 13:07:17$ h and the OSIRIS orange and hydra bands were taken at $T = 13:20:43$ h and $T = 13:21:18$ h, respectively. The histograms were slightly shifted (one-third of the bins width) horizontally for better visualization. The radiance bins used are identical.

to the different spectral bands. Next, we have converted both of them to the NavCam spectral sensitivity by applying multiplicative factors, which were determined as the ratios of the expected spectral radiances in the respective filters. These were computed with equation (2) using the comet spectrum and filter curves in a way analogous to the previous section. Fig. 9 shows the resulting histograms for the example after the transformation of the OSIRIS images to the NavCam spectral sensitivity.

As one can see in Fig. 9, the histograms of hydra and orange bands are now well aligned with each other. The discrepancy between these two bands and the NavCam band is now solely caused by the inaccurate radiometric calibration factor. The next step is to determine the appropriate value of the calibration factor by optimizing the match of the resulting histogram of radiance values with the normalized OSIRIS histograms for the same scene. We have tested factors in an interval ranging from 7.08×10^{-7} to $7.26 \times 10^{-7} \text{Wm}^{-2} \text{sr}^{-1} \text{nm}^{-1} / (\text{DN s}^{-1})$ in steps of $0.01 \times 10^{-7} \text{Wm}^{-2} \text{sr}^{-1} \text{nm}^{-1} / (\text{DN s}^{-1})$ and taken into account all eight

**Figure 9.** Histograms for the example case of Fig. 8 after applying the spectral transformation of the OSIRIS hydra and orange bands to the NavCam spectral range. The histograms were slightly shifted (one-third of the bins width) horizontally for better visualization. The radiance bins used are identical.

NavCam images. For each of the tested values, an average root-mean-square error (RMSE) has been calculated as follows:

$$V_i = \sqrt{\sum (\text{HN}_i - \text{HO}_i)^2}, \quad (6)$$

$$\text{RMSE} = \frac{\sum V_i}{n}, \quad (7)$$

where HN_i and HO_i are the histogram frequencies for the $i = \{1, \dots, 8\}$ pairs of NavCam and OSIRIS images, n is the number of pairs (eight in this case) and RMSE is the average root-mean-square error over all bins. The results are calculated for each value of the calibration factor in the considered interval. The procedure is applied separately to evaluate the {NavCam, hydra} and {NavCam, orange} image sets. The results are shown in Figs 10 and 11, respectively.

The NavCam calibration factor which resulted in the smallest average RMSE was $7.17 \times 10^{-7} \text{Wm}^{-2} \text{sr}^{-1} \text{nm}^{-1} / (\text{DN s}^{-1})$ for the analyses based on both the hydra and orange band. Fig. 12 shows the radiance histograms for the example case resulting with this optimal value of the calibration factor. The distributions of NavCam spectral radiances and normalized OSIRIS hydra and orange spectral radiances are now fully aligned.

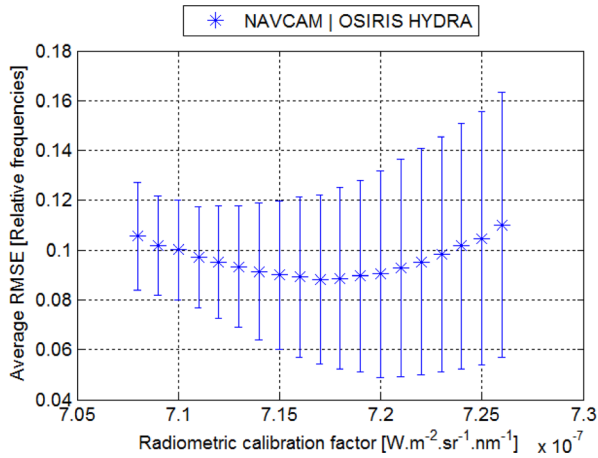


Figure 10. Average RMSE calculated for each tested calibration factor candidate in the interval $[7.08 \times 10^{-7}, 7.26 \times 10^{-7}] \text{ Wm}^{-2} \text{ sr}^{-1} \text{ nm}^{-1} / \text{DN s}^{-1}$ in steps of $0.01 \times 10^{-7} \text{ Wm}^{-2} \text{ sr}^{-1} \text{ nm}^{-1} / (\text{DN s}^{-1})$ considering the Nav-Cam and OSIRIS hydra band pairs. Vertical bars represent the standard deviation of the average RMSE.

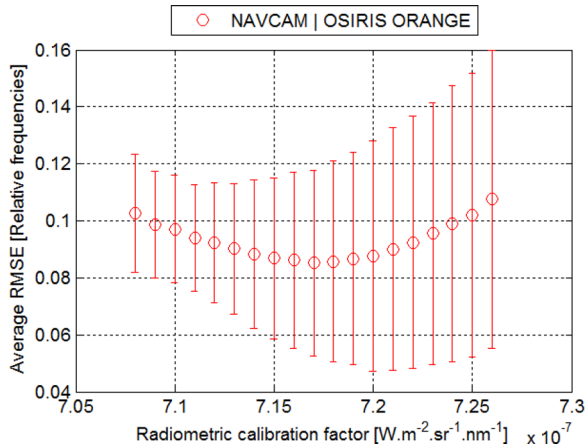


Figure 11. Average RMSE calculated for each tested calibration factor candidate in the interval $[7.08 \times 10^{-7}, 7.26 \times 10^{-7}] \text{ Wm}^{-2} \text{ sr}^{-1} \text{ nm}^{-1} / \text{DN s}^{-1}$ in steps of $0.01 \times 10^{-7} \text{ Wm}^{-2} \text{ sr}^{-1} \text{ nm}^{-1} / (\text{DN s}^{-1})$ considering the Nav-Cam and OSIRIS orange band pairs. Vertical bars represent the standard deviation of the average RMSE.

In order to check a possible dependence on the size of the histogram bins, we repeated the procedure with modified widths of 5×10^{-5} and $2 \times 10^{-4} \text{ Wm}^{-2} \text{ sr}^{-1} \text{ nm}^{-1}$, respectively, which resulted in very similar values of 7.15×10^{-7} and $7.18 \times 10^{-7} \text{ Wm}^{-2} \text{ sr}^{-1} \text{ nm}^{-1} / (\text{DN s}^{-1})$. Hence, there is no indication for a significant influence of the histogram bins. In addition, the radiometric calibration factor estimated with the histogram-based approach is compatible with the one calculated with the mask-based approach $(7.14 \pm 0.07) \times 10^{-7} \text{ Wm}^{-2} \text{ sr}^{-1} \text{ nm}^{-1} / (\text{DN s}^{-1})$, which confirms the robustness of the estimation.

From the results achieved with the mask-based and histogram-based approaches, we conclude that the methodological errors are in the order of 1 per cent (corresponding to the standard deviation over image sets obtained with the mask-based approach). The photometric accuracy of the OSIRIS images used as a reference in this cross-calibration exercise is estimated by Tubiana et al. (2015) to be better than 2 per cent for the visible channels. The nucleus signal

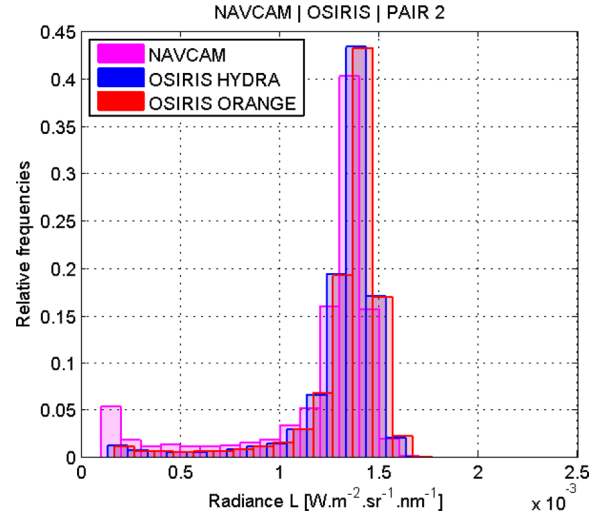


Figure 12. Histograms for the example case of Figs 8 and 9 when applying the radiometric calibration parameter of $7.17 \times 10^{-7} \text{ Wm}^{-2} \text{ sr}^{-1} \text{ nm}^{-1} / (\text{DN s}^{-1})$. The histograms were slightly shifted (one-third of the bins width) horizontally for better visualization. The radiance bins used are identical.

in the NavCam images used for the study is much larger than the values of the subtracted bias fields. The expected uncertainties in the bias and possible thermal contributions to the dark current are smaller than 10 DN (Geiger et al., in preparation) and therefore their contribution to the error budget should be less than 1 per cent. Uncertainties in the spectral sensitivity modelling leading to errors in the computation of the expected average spectral radiance in equation (2) are estimated to be in the order of 4 per cent. Considering the different (uncorrelated) contributions, the relative error of the calibration factor for NavCam images derived in this study is believed to be in the order of 5 per cent.

It should be noted, however, that the accuracy of resulting radiance values critically depends on the scene. Artefact-free images of the nucleus in the same DN range as those used in the present study can indeed be expected to be calibrated with the same quality. However, for lower signals (such as for the coma), the quality of the bias/dark field subtraction is critical. This is discussed in more detail in the paper by Geiger et al. (in preparation), which also includes a description of artefacts present in the images and considerations on temporal stability and point source calibration.

3 DETERMINATION OF THE REFLECTANCE PROPERTIES AS A FUNCTION OF PHASE ANGLE

Next, we apply the results obtained in the previous sections to study the reflectance properties of the comet nucleus as a function of the phase angle (i.e. the angle Sun–comet–spacecraft). We have used the mask-based radiometric calibration factor (cf. equation 4) to convert an extended set of NavCam images acquired at different phase angles from DNs to spectral radiance. Then, we have calculated the radiance factor I/F averaged over the nucleus and studied its phase angle dependence.

We built a catalogue of 594 NavCam images acquired in FOC_ATT/HIGH mode between 2014-07-20 at 06:58:03 h and 2014-08-22 at 08:07:18 h. The uncalibrated images are contained in the MTP005 and MTP006 data sets available in the PSA (Geiger & Barthelemy 2015). From the initial image set, we excluded 36

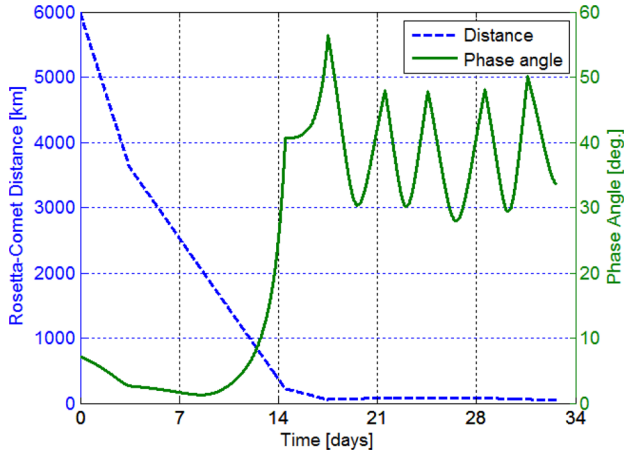


Figure 13. Variation of the phase angle α and the *Rosetta*–comet distance from 2014-07-20 at $T = 0:00:00$ h to 2014-08-22 at $T = 10:00:00$ h.

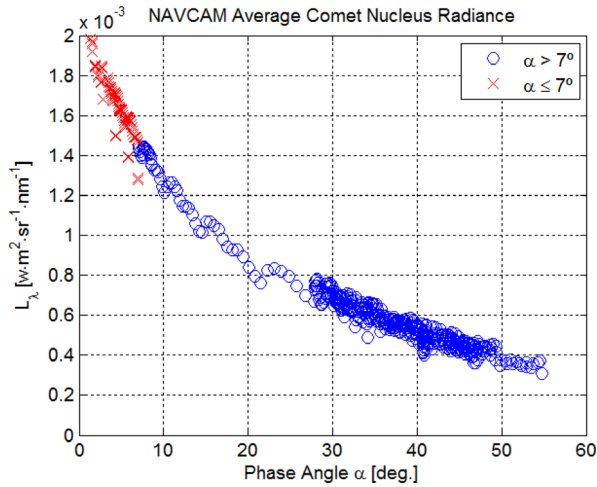


Figure 14. Average comet nucleus spectral radiance L_λ for NavCam images in which the comet nucleus was completely framed, ranging from 2014-07-20 at $T = 06:58:03$ h through 2014-08-22 at $T = 08:07:18$ h.

images which were incomplete or in which the nucleus was not completely framed. As a result, we ended up with 558 processed scenes. The phase angle α ranged from $\sim 1^\circ$ to $\sim 55^\circ$ and the spacecraft–comet distance ranged from ~ 6000 to ~ 50 km during the considered period, as shown in Fig. 13.

Fig. 14 shows the average comet nucleus spectral radiance L_λ versus phase angle α and Fig. 15 shows a plot of the radiance factor I/F , which has been calculated as

$$I/F = \pi \frac{L_\lambda}{E_N}, \quad (8)$$

with

$$E_N = E_0 \left(\frac{d_{sc}}{1 \text{ AU}} \right)^{-2}, \quad (9)$$

where $E_0 = 1.378 \text{ Wm}^{-2}\text{nm}^{-1}$ is the solar spectral irradiance at 1 AU in the effective NavCam band and d_{sc} is the distance from the Sun. Fig. 16 shows the standard deviation of the radiance factor (I/F) over all nucleus pixels. This is a measure of the spatial heterogeneity for each nucleus image.

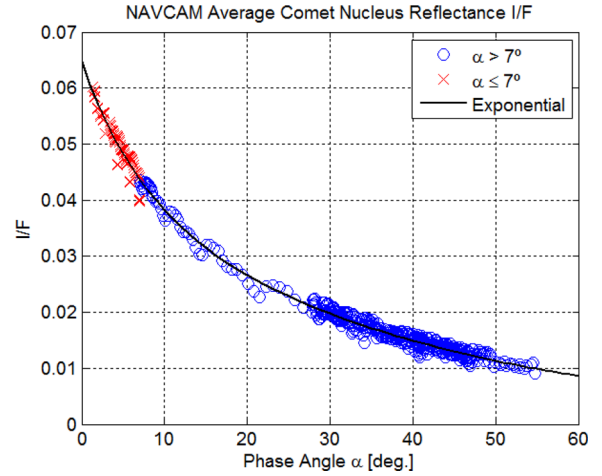


Figure 15. Resulting I/F for 558 NavCam images ranging from 2014-07-20 at $T = 06:58:03$ h through 2014-08-22 at $T = 08:07:18$ h in which the comet nucleus was completely framed. The plain curve shown in the figure is a two-term exponential fit that has been applied to the data points.

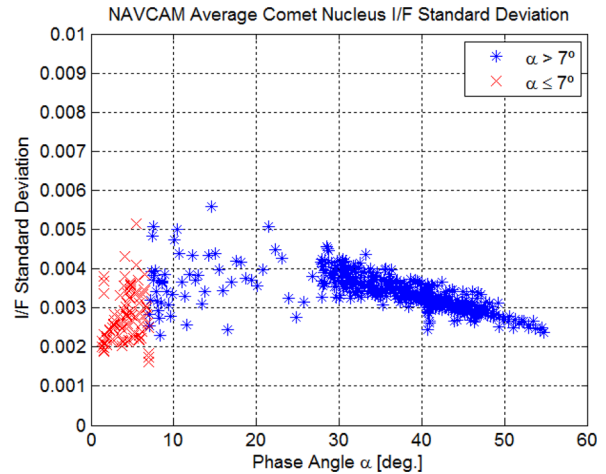


Figure 16. Standard deviation of the radiance factor I/F calculated over the comet nucleus for each image.

As one can see in Figs 14 and 15, the radiance and radiance factor increase strongly due to the opposition effect as the phase angle decreases towards 0° . Some of the data points for $\alpha \leq 7^\circ$ are slightly below the trend, showing smaller values for L_λ and I/F . This is due to the very small size of the comet nucleus with dimensions such as $\sim 15 \times 15$ pixels at the large spacecraft–comet distances when these images were taken between July 20 and 22. Masking and point spread function issues then affect a large fraction of pixels at the border of the nucleus images.

The variability at phase angles between roughly 10° and 27° is due to the rotation of the comet in the corresponding image sequence. It is an indicator of spatial variability at large scales, but it can also be partially caused by shadowing effects. Due to the peculiar shape of the nucleus, the extent of the shadows depends strongly on the side of the comet visible from the spacecraft. With increasing phase angle, shadows become more important and more difficult to account for in the masking process. Nevertheless, the relatively small dispersion of the data points at phase angles larger than 30° (corresponding to many comet rotations) shows that the applied

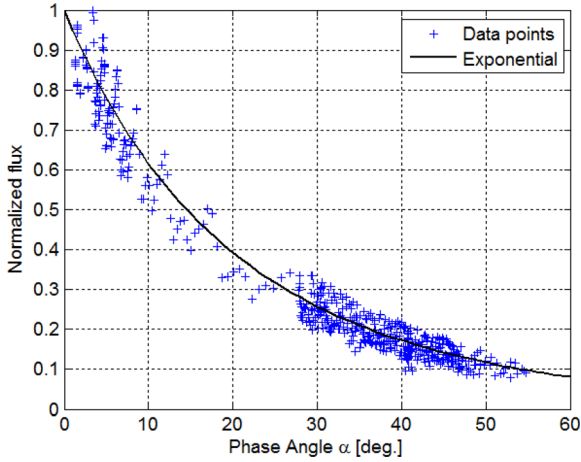


Figure 17. Phase curve of the 67P comet determined from NavCam images with α ranging from $\sim 1^\circ$ to $\sim 55^\circ$. The flux has been normalized and a two-term exponential has been used to fit the data points.

method is still reliable for determining characteristic reflectance properties.

At the smallest measured phase angle of 1.3° , the radiance factor I/F is highest with a value of ~ 0.06 . This is consistent with the results obtained by Fornasier et al. (2015) from OSIRIS data in the orange (649 nm) and hydra (701 nm) filters. VIRTIS measurements presented by Capaccioni et al. (2015) and Ciarniello et al. (2015) are also generally in agreement at the corresponding wavelengths and over a wide range of phase angles.

Fig. 15 also includes a two-term exponential fit to the data points. The resulting value of the geometric albedo (i.e. I/F for the phase angle $\alpha = 0^\circ$) in the broad NavCam filter is 0.065. For comparison, Fornasier et al. (2015) obtained values of 0.0677 and 0.072, respectively, at 649 and 700 nm by fitting a Hapke-model to disc-integrated OSIRIS data. Considering the results of a disc-resolved analysis they quote a value of 0.065 ± 0.002 for the geometric albedo at 649 nm. Based on VIRTIS data Ciarniello et al. (2015) derived an estimate of 0.077 ± 0.002 at 700 nm.

Finally, Fig. 17 depicts the phase curve determined from the series of images. Integrating the measured radiance values over the nucleus image delivers the flux measured at the position of the spacecraft. The flux values were then referenced to constant Sun and spacecraft distances in order to obtain the phase curve. In practice, these steps were achieved by summing up the radiance values and multiplying by the squared spacecraft–comet and comet–Sun distances. The extrapolation to zero phase angle provided by an empirical two-term exponential fit to all data points was used for normalization. The phase curve falls off faster with phase angle than the average radiance factor (Fig. 15) because of the decreasing fraction of illuminated and visible nucleus surface.

The data points in Fig. 17 show a significant dispersion at small phase angles because of the combination of images acquired at different rotation phases. Owing to the variation of the illuminated nucleus cross-section, a separate normalization would be required. However, for this study we did not attempt to quantify the dependence on rotation phase and the applied simplification is believed to be sufficient for determining average quantities. At large phase angles, part of the dispersion of the data points is caused by varying

view zenith angles, and here the simultaneous fit to all data points also provides an azimuthal average of the phase curve.

The Bond albedo can be computed as an integral over the normalized phase curve $\Phi(\alpha)$ multiplied by the geometric albedo (e.g. Hapke 2012):

$$A_{\text{Bond}} = A_{\text{geo}} 2 \int_0^\pi \Phi(\alpha) \sin(\alpha) d\alpha. \quad (10)$$

For objects with irregular shape or heterogeneous surface reflectance, $\Phi(\alpha)$ in this equation represents the azimuthal average. Using the fitted curve as an extrapolation to large phase angles [0° , 180°] we obtained the value of 0.288 for the phase integral and 0.019 for the Bond albedo, which is slightly larger than the values from 0.0157 to 0.0179 given by Fornasier et al. (2015) for wavelength ranges between 649 and 882 nm.

4 CONCLUSIONS

In order to radiometrically calibrate the *Rosetta* NavCam, we carried out a cross-calibration analysis based on OSIRIS-NAC data. The best data set identified for that purpose consists of sequences of images acquired by both cameras on 2014 August 1 shortly before close encounter with the comet. We have used two different methods in this study, one of them based on the average comet nucleus signal (mask-based) and the other one considering the whole range of intensity values as recorded by the camera (histogram-based). Both methods delivered consistent results. For the radiometric calibration factor (converting DN counts into spectral radiance units), we retain a numerical value of $7.14 \times 10^{-7} \text{ W m}^{-2} \text{ sr}^{-1} \text{ nm}^{-1} / (\text{DN s}^{-1})$. This calibration factor value is applicable for images acquired with the attenuation filter (i.e. cover position FOC_ATT) and HIGH gain settings.

Uncertainties in the comparison techniques applied here are in the order of 1 per cent. However, considering contributions from the OSIRIS reference data, bias and dark field subtraction, and spectral sensitivity modelling, we estimate a relative error of 5 per cent for the radiometric calibration. A comprehensive discussion of error estimates and image artefacts will be presented in the forthcoming paper by Geiger et al. (in preparation). That paper will also contain calibration factors applicable for other camera modes and a description of processing steps applied for generating ‘Level 3’ data sets for the PSA. The availability of calibrated NavCam images will facilitate quantitative analyses and enhance the scientific value of the data.

Finally, we applied the radiometric calibration to a series of NavCam images taken at phase angles between $\sim 1^\circ$ and $\sim 55^\circ$. By means of empirical fits to the phase angle dependence of the radiance factor and the phase curve (normalized flux), we determined values of 0.065 ± 0.003 for the geometric albedo and 0.019 ± 0.001 for the Bond albedo. Here, the error estimates account for the 5 per cent relative error in the calibration, without attempting to quantify uncertainties in the model fits. These values are broadly consistent with published results derived from OSIRIS and VIRTIS measurements in the corresponding wavelength range, which corroborates the validity of the calibration results.

ACKNOWLEDGEMENTS

Rosetta is an ESA mission with contributions from its member states and NASA. Rosetta’s Philae lander is provided by a consortium led by DLR, MPS, CNES and ASI. The work described in this paper was started at the COSPAR Capacity Building Workshop for Planetary

Missions Data Analysis held from 2015 October 26 to November 6 in Guaratinguetá, Brazil. We thank Holger Sierks for approving access to the OSIRIS image data before their official release in the PSA.

REFERENCES

- Capaccioni F. et al., 2015, *Science*, 347, 6220, aaa0628
- Castellini F., Antal-Wokes D., Pardo de Santayana R., Vantournhout K., 2015, Proc. 25th Int. Symp. Space Flight Dyn., Munich, Germany
- Ciarniello M. et al., 2015, *A&A*, 583, A31
- Feldman P. et al., 2015, *A&A*, 582, A8
- Fornasier S. et al., 2015, *A&A*, 583, A30
- Geiger B., 2016, *Acta Astronaut.*, 126, 475
- Geiger B., Barthelemy M., 2015, ROSETTA ORBITER NAVCAM PRL-MTP005/MTP006, RO-C-NAVCAM-2-PRL-MTP005-V1.0, RO-C-NAVCAM-2-PRL-MTP006-V1.0, ESA Planetary Science Archive and NASA Planetary Data System. Available at: <ftp://psa.esac.esa.int/pub/mirror/INTERNATIONAL-ROSETTA-MISSION/NAVCAM/>
- Geiger B., Barthelemy M., Archibald C., 2016, Rosetta Navigation Camera Experiment to Archive Interface Control Document, Version 5.3. Available at: <ftp://psa.esac.esa.int/pub/mirror/INTERNATIONAL-ROSETTA-MISSION/NAVCAM/RO-C-NAVCAM-2-EXT3-MTP035-V1.0/DOCUMENT/RO-SGS-IF-0001.PDF>
- Grün E. et al., 2016, *MNRAS*, 462, S220
- Gutierrez-Marques P. et al., 2015, ROSETTA ORBITER PRELANDING OSINAC 3 RDR DATA MTP 006 V1.0, RO-C-OSINAC-3-PRL-67PCHURYUMOV-M06-V1.0, ESA Planetary Science Archive and NASA Planetary Data System
- Hapke B., 2012, *Theory of Reflectance and Emittance Spectroscopy*. Cambridge Univ. Press, Cambridge
- Keller H. U., 2007, *Space Sci. Rev.*, 128, 433
- Otsu N., 1979, *Man and Cybern.*, 9, 62
- Pardo de Santayana R., Lauer M., 2015, Proc. 25th Int. Symp. Space Flight Dyn., Munich, Germany
- Serra J., 1982, *Image Analysis and Mathematical Morphology*. Academic Press, London
- Sierks H. et al., 2015, *Science*, 347, 6220, aaa1044
- Tubiana C. et al., 2015, *A&A*, 583, A46
- Vincent J.-B. et al., 2016, *MNRAS*, 462, S194

This paper has been typeset from a $\text{\TeX}/\text{\LaTeX}$ file prepared by the author.